Research Article

Journal of Environmental Nanotechnology

Green Synthesis, Characterization and Process Optimization of a *Clerodendrum inerme*-Mediated ZnO/g-C_3N_4 Heterojunction for Congo Red Photodegradation

Snehal K. Kamble[1], Anju Rani[2*], Muthukumaran Kannan[3], G. Magudeeswaran[4], D. Sathish Kumar[5] and Rajasekaran Saminathan[6]

[1]Department of Physics, Yeshwantrao Chavan College of Engineering, Nagpur, Wanadongri, MH, India
[2]Department of Physics, School of Engineering and Technology, CGC University, Mohali, PB, India
[3]Department of Biomedical Engineering, Dhanalakshmi Srinivasan College of Engineering and Technology, Mamallapuram, Chennai, TN, India
[4]Department of Mechanical Engineering, P S N A College of Engineering and Technology, Dindigul, TN, India
[5]Department of Mechanical Engineering, Nehru Institute of Engineering and Technology, Coimbatore, TN, India
[6]Department of Mechanical Engineering, College of Engineering and Computer Science, Jazan University, Saudi Arabia
Received: 06.08.2026 Accepted: 31.08.2026 Published: xx.xx.xxxx
*anjurani3696@gmail.com

ABSTRACT

The aim of this study was to develop an environmentally sustainable ZnO/g-C_3N_4 heterojunction photocatalyst for visible-light degradation of Congo red using *Clerodendrum inerme* leaf extract as a green complexing and growth-controlling medium. To address the limitations associated with conventional chemical synthesis and rapid photogenerated charge-carrier recombination, ZnO was coupled with thermally prepared g-C_3N_4 through a plant-assisted route and characterized by XRD, FTIR, SEM–EDX, UV–Vis DRS, and BET analyses. XRD confirmed the coexistence of hexagonal wurtzite ZnO and layered g-C_3N_4 without detectable crystalline impurities, while the ZnO crystallite size decreased from approximately 24.8 nm to 17.6 nm following composite formation. The apparent optical bandgap values were approximately 3.20, 2.68, and 3.13 eV for ZnO, g-C_3N_4, and ZnO/g-C_3N_4, respectively, while the BET surface area increased from 90.0 to 107.0 $m^2\ g^{-1}$. Under visible-light LED irradiation, ZnO/g-C_3N_4 achieved approximately 87% Congo red degradation within 120 min compared with 65% for g-C_3N_4. The degradation followed pseudo-first-order kinetics, and scavenger experiments identified superoxide radicals as the dominant reactive species, with photogenerated holes and hydroxyl radicals also contributing. These findings demonstrate the potential of *Clerodendrum inerme*-mediated ZnO/g-C_3N_4 for photocatalytic treatment of dye-contaminated wastewater. Future investigations should evaluate mineralization efficiency, repeated-use stability, catalyst leaching, toxicity, and performance in real industrial wastewater containing mixed contaminants.

Keywords: Green synthesis; Photocatalyst; Optical bandgap; Absorption; Congo-red; Wastewater.

1. INTRODUCTION

Water pollution caused by synthetic dyes and industrial effluents poses a significant environmental challenge due to the persistence, toxicity, and poor biodegradability of these contaminants. Among them, Congo red (CR), a stable azo dye widely discharged from textile, leather, pharmaceutical, and chemical industries, is particularly difficult to remove from wastewater. Heterogeneous photocatalysis emerged as an effective and sustainable approach for degrading such pollutants through the generation of ROS under light irradiation. Zinc oxide (ZnO) is a promising photocatalyst due to its high electron mobility, chemical stability, and low toxicity; however, rapid electron-hole recombination and a wide bandgap limit its visible-light activity. Graphitic carbon nitride (g-C_3N_4), a metal-free visible-light-responsive semiconductor, effectively overcomes these limitations by forming ZnO/g-C_3N_4 heterojunctions that improve charge separation, broaden visible-light absorption, and improve photocatalytic efficiency. Phytoextract-mediated ZnO-doped g-C_3N_4 synthesized by Ficus benjamina leaf extract exhibited significantly enhanced photocatalytic degradation of MB and auramine orange dyes, together with improved antibacterial activity against Escherichia coli (Dahiya *et al.* 2023).

Green synthesis has become more environmentally sustainable than conventional chemical methods because plant-derived phytochemicals act as reducing, capping, and stabilizing agents during nanoparticle fabrication. Plant-mediated synthesis eliminates the need for hazardous chemicals while reducing energy consumption and improving environmental compatibility. A comprehensive review

highlighted that phytochemical-assisted green synthesis produces nanoparticles with excellent antibacterial, antioxidant, anticancer, and anti-inflammatory activities while emphasizing the importance of systematic characterization and toxicity assessment for future biomedical applications (Mohanta *et al.* 2023).

Among medicinal plants, *Clerodendrum inerme* has emerged as an attractive biological resource because it contains abundant flavonoids, phenolics, terpenoids, and other bioactive metabolites capable of facilitating nanoparticle synthesis. Silver nanoparticles synthesized using *Clerodendrum inerme* demonstrated potent insecticidal activity against Stomoxys calcitrans through acetylcholinesterase inhibition while maintaining acceptable safety toward beneficial parasitoids and earthworms (Alasmari *et al.* 2025). Green synthesis of MgO using *Clerodendrum inerme* bast fiber produced highly crystalline and porous nanoparticles exhibiting excellent thermal stability together with remarkable antibacterial activity against Pseudomonas aeruginosa (Ganvir *et al.* 2026).

Numerous green-synthesized semiconductor photocatalysts have demonstrated remarkable efficiency for Congo red degradation under visible-light irradiation. Fe/carbon sphere-modified TiO_2 photocatalysts achieved 95% degradation of Congo red together with efficient removal of pharmaceutical contaminants while maintaining excellent reusability (Langa *et al.* 2026). Green-synthesized NiO /TiO_2 nanoparticles prepared using Tribulus terrestris/ Calotropis gigantea leaf extract effectively degraded Congo red while simultaneously exhibiting antibacterial, antifungal, and antioxidant activities (Khan *et al.* 2021). Biosynthesized Ag/Pd bimetallic nanoparticles prepared using diatom algae extract exhibited superior photocatalytic degradation of azo dyes, while Response Surface Methodology provided excellent process optimization with an R^2 value of 0.9838 (Al-Enazi, 2022). Green-synthesized Fe_3O_4 nanoparticles using Dendrophthoe falcata leaf extract demonstrated enhanced Congo red degradation together with outstanding anti-inflammatory activity (Anuradha *et al.* 2025).

Silver oxide-decorated rGO composites exhibited efficient visible-light degradation of Congo red while simultaneously possessing antibacterial and antioxidant activities (Lekshmi *et al.* 2022). Green-fabricated α-Bi_2O_3 nanoparticles synthesized using Rubus ellipticus extracts achieved 89.2% Congo red degradation under visible-light irradiation while exhibiting broad-spectrum antibacterial activity (Chauhan *et al.* 2024). Mn-doped ZnO nanoparticles synthesized using *Ipomoea staphylina* leaf extract achieved 92% Congo red degradation and demonstrated superior photocatalytic performance compared with pristine ZnO nanoparticles (Senthilkumar and Govindasamy, 2024). Green-synthesized ZnO nanoparticles prepared by *Moringa oleifera* extract exhibited the highest methyl orange degradation efficiency together with excellent surface-enhanced Raman sensing capability (Kashyap *et al.* 2026). Green-synthesized ZnO nanoparticles by Azadirachta indica leaf achieved degradation efficiencies of 95.35% for methyl orange, 97.82% for methylene blue, and 98.29% for Congo red while also rapidly reducing p-nitrophenol to p-aminophenol (Amale *et al.* 2026).

Although plant-mediated metal-oxide photocatalysts and ZnO/g-C_3N_4 composites have been extensively investigated, several research gaps remain. First, previous phyto-mediated ZnO/g-C_3N_4 studies have primarily employed other botanical sources, such as *Ficus benjamina*, and have mainly focused on pollutants such as methylene blue and auramine orange rather than Congo red (Dahiya *et al.* 2023). Second, although *Clerodendrum inerme* contains phenolic, flavonoid, terpenoid, and other phytochemical constituents capable of participating in nanoparticle formation, its application as a green mediator for controlling ZnO formation on g-C_3N_4 and producing a photocatalytically active heterojunction remains insufficiently explored. Third, many green-photocatalyst studies report dye-removal efficiency under selected experimental conditions without simultaneously correlating structural, optical, morphological, and surface characteristics with operational parameters, reaction kinetics, and reactive-species behaviour. Consequently, an integrated investigation combining green heterojunction synthesis, physicochemical characterization, systematic process-variable evaluation, kinetic modelling, and radical-trapping analysis is still required for Congo red remediation. To address these gaps, the present study reports, to the best of our knowledge, the first *Clerodendrum inerme* leaf-extract-assisted preparation of ZnO-functionalized g-C_3N_4 for visible-light-driven Congo red degradation. The novelty of this work lies in integrating an environmentally compatible synthesis route with XRD, FTIR, SEM–EDX, UV–Vis DRS, and BET characterization and systematically evaluating the effects of initial Congo red concentration, photocatalyst dosage, solution pH, reaction temperature, and stirring rate. In addition, pseudo-first-order kinetic analysis and reactive-species scavenging experiments were employed to identify the dominant oxidative species and clarify the heterojunction-assisted degradation mechanism. This integrated approach provides a more comprehensive assessment of the structural–performance relationship and practical potential of the developed photocatalyst for treatment of dye-containing wastewater.

2. MATERIALS AND EXPERIMENTAL PROCEDURES

2.1 Chemicals and Raw Materials

Fresh *Clerodendrum inerme* leaves, zinc nitrate hexahydrate [$Zn(NO_3)_2 \cdot 6H_2O$, 99%], ethanol (99.5%), Congo red ($C_{32}H_{22}N_6Na_2O_6S_2$, 99%), melamine ($C_3H_6N_6$, 99%), sodium hydroxide (NaOH, 98%), and distilled water were employed to make ZnO/g-C_3N_4 and conduct photocatalytic experiments.

2.2 Green Preparation of the ZnO/g-C_3N_4 Heterojunction

2.2.1 Preparation of *Clerodendrum inerme* Leaf Extract

Fresh *Clerodendrum inerme* leaves were collected from a cultivated garden following applicable guidelines. The leaves were rinsed thoroughly with tap water and subsequently with distilled water to remove surface contaminants. The leaves were shade-dried under clean, ventilated conditions and ground into a fine powder. Five grams of the resulting powder were dispersed in 100 mL of deionized water and heated at 60 °C for 3 h under magnetic stirring (Alasmari *et al.* 2025a). After reaching room temperature, the suspension was passed through filter paper to obtain a clear plant extract. Freshly prepared filtrate was immediately utilized for photocatalyst synthesis.

Bulk g-C_3N_4 was produced from melamine at 550 °C for 4 h in a covered ceramic crucible, followed by cooling and grinding. For ZnO formation, 2.97 g of $Zn(NO_3)_2 \cdot 6H_2O$ was dissolved in 100 mL of DIW under stirring to prepare a 0.1 M precursor solution. The plant extract was gradually introduced into this solution, followed by dropwise addition of NaOH until pH 10 was reached. Subsequently, the prepared g-C_3N_4 powder was dispersed in the reaction mixture and continuously stirred to promote ZnO deposition over its surface, producing a ZnO/g-C_3N_4 heterojunction precursor.

2.3 Plant-assisted Synthesis of ZnO and ZnO/g-C_3N_4 Photocatalysts

For ZnO preparation, *Clerodendrum inerme* leaf extract was introduced gradually into the 0.1 M zinc nitrate solution while maintaining the temperature at 70 °C under continuous magnetic stirring. Sodium hydroxide solution was subsequently added dropwise until the mixture reached pH 10. The appearance of a whitish precipitate indicated the formation of the zinc-containing intermediate. Stirring was continued for 3 h to facilitate complete precipitation.

Previously prepared g-C_3N_4 powder was ultrasonically dispersed in distilled water and incorporated into the zinc precursor mixture before pH adjustment. The suspension was stirred at 70 °C for 3 h to promote uniform nucleation and deposition of ZnO particles on g-C_3N_4 sheets. The recovered products were filtered and repeatedly rinsed with ethanol and distilled water. Both samples were oven-dried at 80 °C for 12 h. ZnO was calcined at 450 °C for 2 hour, whereas the composite was treated at 400 °C for 2 h to raise crystallinity while preserving the g-C_3N_4 framework (Van Thuan *et al.* 2022). Figure 1 illustrates the green preparation pathw

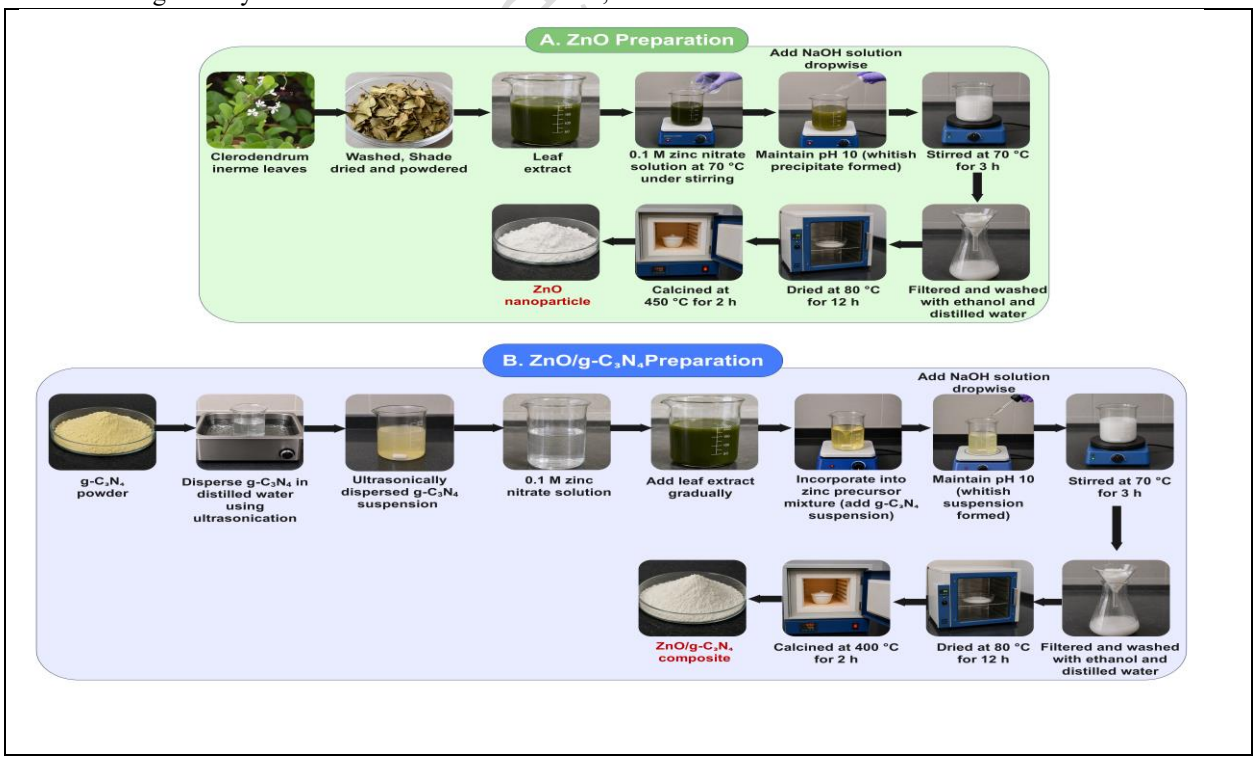

Fig. 1: Green synthesis pathway of *Clerodendrum inerme*-mediated ZnO/g-C_3N_4 photocatalysts

2.4 Characterization Methods

The physicochemical characteristics of the prepared photocatalysts were evaluated using complementary analytical methods. Crystalline phases was identified by PANalytical X'Pert PRO diffractometer (Khawale *et al.* 2024). Surface functional groups were examined using a PerkinElmer Spectrum Two FTIR spectrometer within 4000–400 cm^{-1}. Surface structure and particle distribution were investigated using a Zeiss, Gemini FESEM operated at 15 kV and working distance of 10 mm (Prisrin *et al.* 2022). Micrographs recorded at nearly 15,000× magnification were used to assess agglomeration, surface texture, and morphological differences between ZnO and ZnO/g-C_3N_4. Elemental composition determined by Oxford Instruments EDS detector coupled with microscope. Pore characteristics and specific surface area measured by N_2 adsorption–desorption using a Micromeritics ASAP 2020 analyser. Diffuse-reflectance spectra and optical bandgaps were obtained by Shimadzu UV-2600 equipped with ISR-2600Plus sphere

2.5 Photocatalytic Experimental Procedure

Photocatalytic experiments were performed in a 100 mL borosilicate-glass reactor using Congo red as the target contaminant. In each trial, 40 mg of photocatalyst was suspended in 50 mL of Congo red solution with a concentration of 50 mg L^{-1} (Langa *et al.* 2025). The suspension was stirred in the dark for 40 min to attain adsorption–desorption equilibrium. It was subsequently irradiated using a 15 W white LED lamp producing approximately 1000 lm across the visible region of 400–700 nm. Separation between the light source and the reaction vessel was maintained at 12 cm.

A circulating water bath maintained the suspension temperature at 30 ± 0.5 °C, preventing heating caused by prolonged illumination. Samples were withdrawn at predetermined intervals, centrifuged to separate ZnO/g-C_3N_4 particles, and analysed at the maximum absorption wavelength of Congo red (approximately 497 nm) by a Thermo Scientific UV–Visible spectrophotometer. Dye-removal efficiency was calculated as follows:

$$\text{Degradation efficiency } (\%) = \frac{U_0 - U_t}{C_0} \times 100 \quad \ldots (1)$$

where C_0 shows Congo red concentration after dark equilibration and C_t corresponds to its concentration after an irradiation period t.

3. RESULTS AND DISCUSSION

3.1 Characterization

3.1.1 XRD Investigation

Fig. 2 presents XRD recorded by PANalytical X'Pert PRO diffractometer. ZnO exhibited characteristic reflections at 2θ values of 31.72°, 34.37°, 36.20°, 47.49°, 56.55°, 62.81°, 67.91°, and 69.05°, indexed to (100), (002), (101), (102), (110), (103), (112), and (201). The g-C_3N_4 pattern displayed peaks near 13.05° and 27.32°, assigned to the (100) in-plane arrangement and (002) stacking, respectively. Both sets of reflections were retained in the composite, verifying successful heterojunction formation without detectable crystalline impurities.

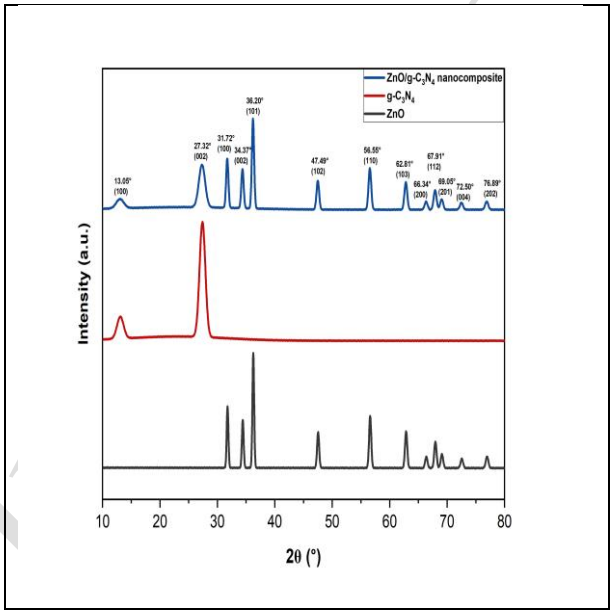

Fig. 2: XRD profiles of ZnO, g-C_3N_4, and ZnO/g-C_3N_4 photocatalysts

The ZnO displayed intense peaks at approximately 31.72°, 34.37°, 36.20°, 47.49°, 56.55°, 62.81°, 67.92°, and 69.05°, corresponding to (100), (002), (101), (102), (110), (103), (112), and (201) hexagonal wurtzite ZnO, respectively. No distinct impurity reflections associated with unreacted zinc precursors or other zinc-containing phases were detected, indicating satisfactory phase purity.

The g-C_3N_4 sample exhibited two characteristic reflections at nearly 13.05° and 27.32°. The weaker (100) reflection originated from the arrangement of tri-s-triazine units, whereas the prominent (002) peak represented stacking of aromatic layers. In a ZnO/g-C_3N_4 profile, the principal reflections of both components remained detectable, confirming successful composite formation without altering their fundamental crystal structures. The peak positions and JCPDS assignments obtained here (ZnO: 31.72°, 34.37°, 36.20°, 47.49°, 56.55°, 62.81°, 67.91°, 69.05°; g-C_3N_4: 13.05°, 27.32°) closely match those reported for g-C_3N_4/ZnO heterostructures, where ZnO reflections at 31.76°, 34.31°, 36.1°, 47.54°, 56.57°, 62.9°, and 67.82° (JCPDS No. 36-1451) and g-C_3N_4 reflections at 13.1° and 27.3°

(JCPDS No. 87-1526) were similarly indexed (Mathialagan *et al.* 2020).

A slight reduction in peak intensity and moderate broadening were observed after coupling. These changes can be associated with smaller coherent crystalline domains, interfacial interactions, and the dispersion of ZnO crystallites across the layered g-C_3N_4 surface. Minor positional variations in the composite peaks may indicate interfacial strain rather than substitution of Zn or O atoms into the g-C_3N_4 framework. Absence of additional diffraction peaks further suggests that heterojunction formation did not generate measurable crystalline by-products.

Average crystallite size was estimated by the Debye-Scherrer relationship:

$$D = \frac{0.9\lambda}{\beta \cos\theta} \quad \ldots (2)$$

The calculated crystallite sizes were approximately 24.8 nm for ZnO and 17.6 nm for ZnO within $ZnO/g - C_3\ N_4$ composite, indicating restricted crystal growth following heterojunction formation.

3.1.2 FTIR Investigation

The FTIR spectra of *Clerodendrum inerme* leaf extract, g-C_3N_4, and the unused ZnO/g-C_3N_4 photocatalyst were plotted as obtained using a PerkinElmer Spectrum Two spectrometer. The plant extract shows a broad band at 3380 cm-1, which is due to the stretching vibrations of O-H and N-H of phenolic and amine compounds. Other bands at 2920, 1734, 1628, 1250, and 1084 cm−1 were attributed to the aliphatic C–H stretching, carbonyl C=O stretching, aromatic C=C/C=N stretching, C–O stretching, and C–O–C vibration, respectively. The presence of these functional groups suggests that plant-based compounds are able to complex zinc ions and regulate particle growth.

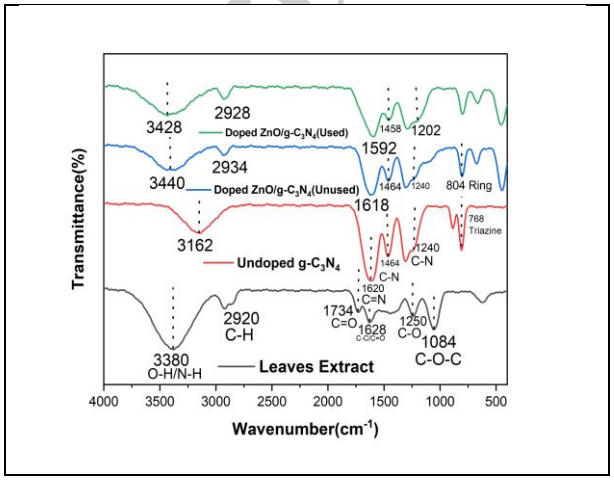

Fig. 3: FTIR of extract and fresh-and-recovered composites

The g-C_3N_4 spectrum showed a broad band around 3162 cm^{-1}, which is attributed to the presence of some N–H groups and absorbed water. Bands at ~1620, 1464 and 1240 cm^{-1} assigned to the C=R stretching and C–N stretching of the aromatic C–N framework in the conjugated system. A clear peak was observed around 768 cm^{-1}, which could be assigned to a breathing vibration.

An g-C_3N_4 bands were still distinguishable from the unused ZnO/g-C_3N_4 photocatalyst after the formation of heterojunction. The bands at 3440, 2934, 1618, 1464, 1240 and 804 cm^{-1} were assigned to the vibrations of O–H/N–H, aliphatic C–H, C=N, aromatic C–N, bridging C–N and tri-s-triazine rings, respectively. The slight shifts in their intensity and position suggest the interfacial interactions between ZnO and g-C_3N_4. Absorptions were observed in the lower wavenumbers (430-560 cm^{-1}) and were attributed to the vibrations of the Zn–O lattice, thus confirming the presence of ZnO in the composite.

The main structural bands, which were around 3428, 2928, 1592, 1458, and 1202 cm^{-1} of recovered ZnO/g-C_3N_4, indicated good structural stability after photocatalytic application. The changes in the C–N framework bands from 1618 to 1592 cm^{-1}, 1464 to 1458 cm^{-1}, and 1240 to 1202 cm^{-1} might be due to the presence of residual aromatic, azo, and sulfonate intermediate species formed during the degradation of Congo red. Different O–H/N–H and C–N region data also suggest interactions between pollutant molecules, photocatalytic surface sites, and degradation products. The FTIR bands identified for g-C_3N_4 and the ZnO/g-C_3N_4 composite in this study (C–N and C=N stretching near 1618–1240 cm^{-1}, tri-s-triazine ring breathing near 768–804 cm^{-1}, and a broad O–H/N–H band above 3000 cm^{-1}) are consistent with reported assignments for ZnO/g-C_3N_4 heterojunctions, where analogous peaks at 1232 and 1640 cm^{-1} were attributed to C–N and C=N stretching, 810 cm^{-1} to the s-triazine ring breathing mode, and 3000–3400 cm^{-1} to N–H/O–H stretching vibrations (Hassan *et al.* 2024).

3.1.3 SEM Investigation

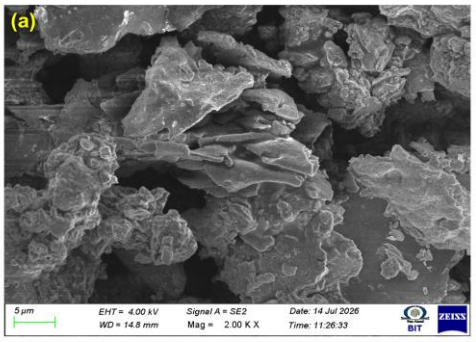

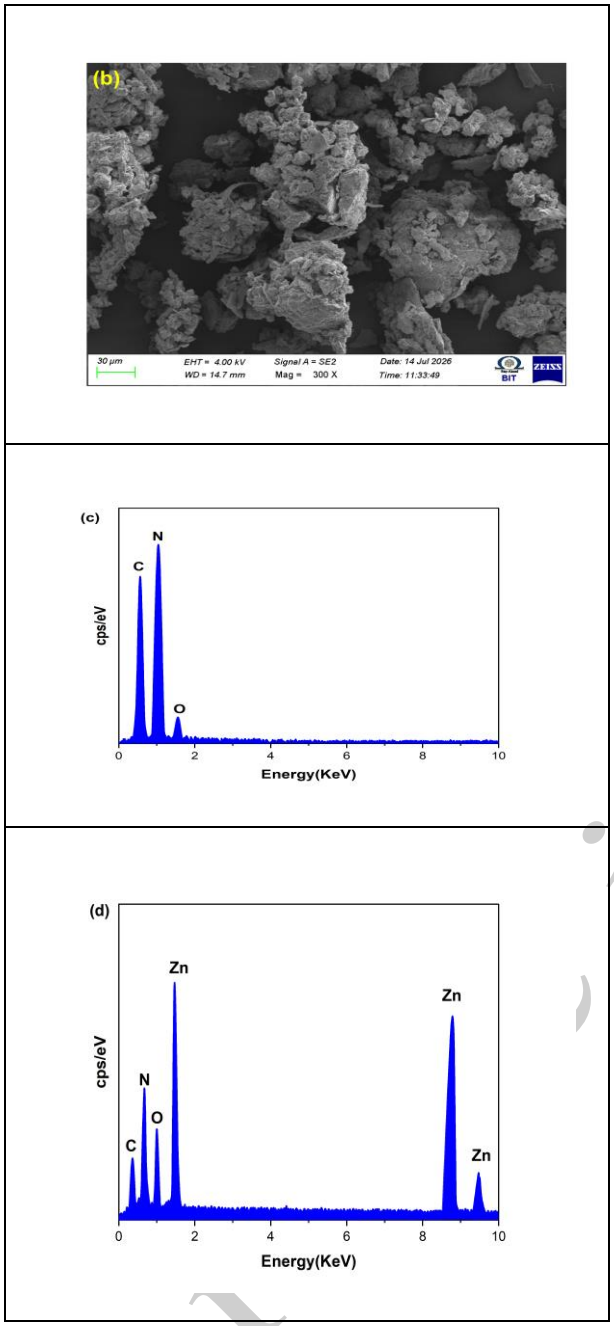

Fig. 4: SEM micrographs (a) ZnO and (b) ZnO/g-C_3N_4, with EDX of (c) ZnO and (d) ZnO/g-C_3N_4

The morphology of *Clerodendrum inerme-mediated ZnO and the ZnO/g-C_3N_4 composite was displayed using SEM morphology, as shown in Fig. 4. Figure 4(a), recorded at 2.00 k× magnification, exhibits densely packed, irregular aggregates containing overlapping plate-like structures, rough surfaces,* and interconnected voids. The distinct layer structure is more frequently observed in a composite with g-C_3N_4 than in pure ZnO. Some plate-like areas also show fine granular deposits, though it is not possible to confirm the nature of these deposits from the SEM image alone, as these are likely to be ZnO.

Figure 4(b) (300× magnification) reveals the presence of micron-scale small agglomerates in a widely dispersed distribution, with irregular shapes, heterogeneous surfaces, and large inter-aggregate spaces. The low magnification prevents the resolution of individual particles of ZnO, g-C_3N_4 sheets and their contact points. In addition, the magnification and scale bars of the figures vary. To confirm the sample assignments and formation of the ZnO/g-C_3N_4 heterojunction, higher-magnification images captured under the same conditions were needed, in addition to acquiring elemental mapping images of the Zn, O, C, and N elements. In previous studies, reported SEM investigations of g-C_3N_4/ZnO composites indicate that ZnO particle size and morphology are strongly influenced by hydrothermal synthesis conditions, with smaller particles and cone-like edge structures forming on g-C_3N_4 at higher hydrothermal pH values (Utomo *et al.* 2024).

3.1.4 EDX Investigation

Elemental composition was determined using an Oxford Instruments EDX detector coupled to the microscope. The ZnO spectrum in Fig. 4c showed dominant zinc and oxygen signals, confirming the expected elemental composition. A weak carbon signal may originate from the conductive mounting tape or residual plant-derived compounds.

The composite spectrum in Fig. 4d contained zinc, oxygen, carbon, and nitrogen peaks. The simultaneous detection of these elements verifies the coexistence of ZnO and g-C_3N_4 within the analysed region. No prominent unexpected elemental signals was observed, showing satisfactory purity of prepared material. EDX confirms elemental presence but does not independently establish chemical bonding or lattice incorporation.

3.1.5 Optical Properties

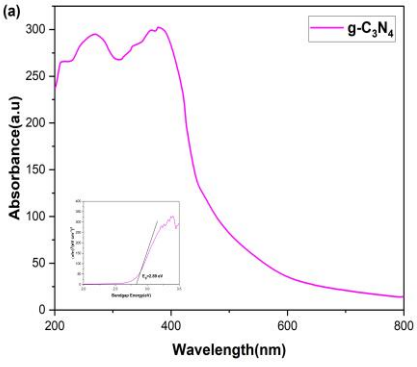

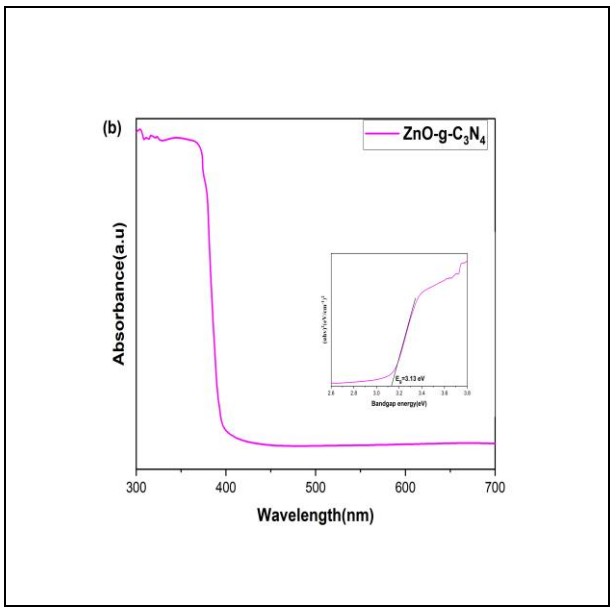

Fig. 5: (a) g-C_3N_4 and (b) ZnO/g-C_3N_4 optical diffuse-reflectance and Tauc plots

Table 1. EDX-derived elemental composition of the synthesized heterojunction photocatalysts

Sample	Element	Mass (%)	Atomic (%)
ZnO/g-C3N4	Zinc	39.50	12.18
	Oxygen	18.80	23.69
	Carbon	17.20	28.87
	Nitrogen	24.50	35.26
	Total	100.00	100.00
g-C3N4	Carbon	38.60	42.44
	Nitrogen	58.70	55.33
	Oxygen	2.70	2.23
	Total	100.00	100.00

Optical response of $ZnO/g-C_3N_4$ and $g-C_3N_4$ were examined from 200 to 800 nm by Shimadzu spectrophotometer fitted with ISR-2600Plus. As illustrated in Fig. 5, $g-C_3N_4$ displayed an absorption edge near 463 nm, whereas the composite showed an edge extending to approximately 396 nm. This shift indicates improved visible-light utilization after establishing interfacial contact between ZnO and $g-C_3N_4$. Bandgap energies were evaluated from linear regions of the Tauc plots using the Kubelka-Munk-transformed reflectance data:

$$[F(R)h\nu]^n = A(h\nu - E_g) \quad \ldots (3)$$

where $F(R), h\nu, A$,and E_g represent the Kubelka-Munk function, photon energy, proportionality constant and optical bandgap, respectively. The estimated bandgaps were approximately 2.68 eV for $g-C_3N_4$ and 3.13eV for $ZnO/g-C_3N_4$. The lower apparent bandgap and extended absorption of the composite favour visible-light excitation. More importantly, $ZnO/g-C_3N_4$ interface promotes charge-carrier separation and reduces recombination, thereby improving reactive-species generation during Congo red degradation. In a previous study, a ZnO-doped g-C3N4 S-scheme heterojunction photocatalyst achieved complete degradation of 1.0 mg L^{-1} deoxynivalenol within 3 h under UV irradiation, where the enhanced photocatalytic activity was attributed to efficient charge separation (Hao *et al.* 2026).

3.1.6 Surface-area and Pore Analysis

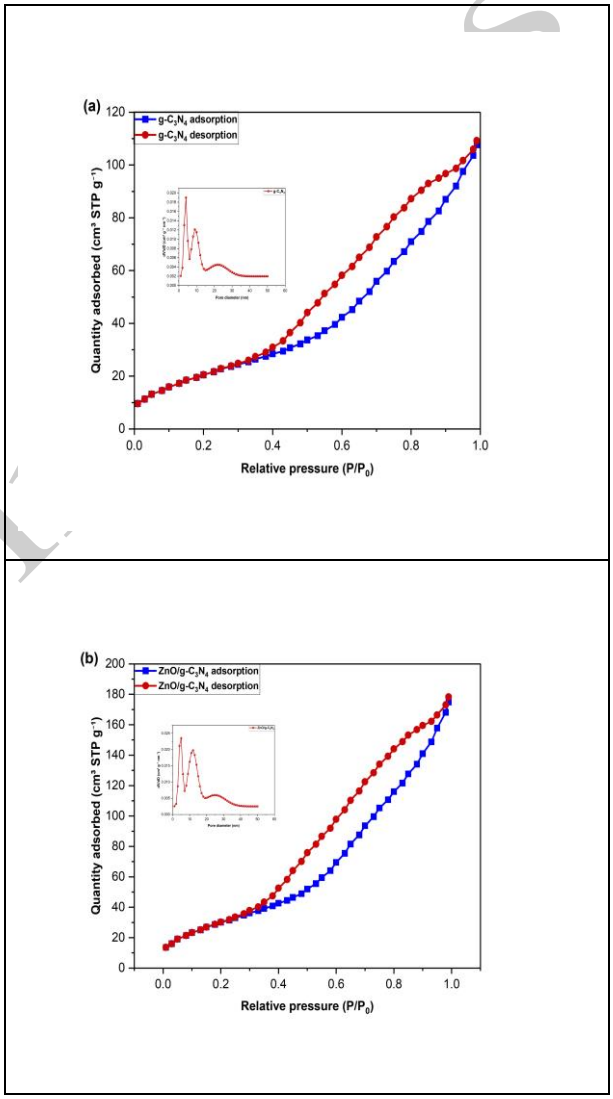

Fig. 6: Nitrogen sorption and pore-size profiles

Before measurement, samples were degassed at 120 °C to eliminate adsorbed moisture. As presented in Fig. 6, both materials produced Type IV adsorption–desorption at H3-type loops, showing predominantly mesoporous structures containing slit-shaped pores associated with layered particle assemblies.

BET surface area of g-C3N4 was 90.0 $m^2\ g^{-1}$, while ZnO/g-C3N4 showed a higher value of 107.0 $m^2\ g^{-1}$.

Its total pore volume also increased from 0.167 to 0.275 $cm^3\ g^{-1}$. This textural improvement may result from ZnO dispersion over the layered g-C_3N_4 surface, which restricts sheet restacking and generates additional interfacial cavities. The larger accessible surface provides more adsorption and reaction sites, improving contact among the photocatalyst, Congo red molecules, and visible-light-generated reactive species. Similarly, Green-synthesized CuO–ZnO–carbon nanocomposites using waste Tagetes flower petals exhibited outstanding adsorption capacities of 331.36 mg g^{-1} for Congo red dye after CTAB surface modification, owing to their enhanced surface area, and surface functionality, demonstrating excellent potential for wastewater remediation (Prajapati and Mondal, 2021).

Table 2. Comparative surface area and characteristics

Parameter	ZnO/g-C_3N_4	g-C_3N_4
BJH average pore diameter (nm)	16.0	12.0
Total pore volume ($cm^3\ g^{-1}$)	0.275	0.167
BET surface area ($m^2\ g^{-1}$)	107.0	90.0

3.2 Photocatalytic Performance

Photocatalytic removal of Congo red under visible LED irradiation was examined. Effects of photocatalyst solution pH, irradiation time, dosage, temperature, catalyst reuse, and initial pollutant concentration were systematically evaluated. Rapid removal occurred during the initial irradiation period because numerous surface-active sites were available and the pollutant concentration was comparatively high. The reaction gradually slowed as Congo red was consumed and transformation intermediates competed for available surface sites.

After 120 min, the ZnO/g-C_3N_4 composite reached approximately 87% degradation, whereas g-C_3N_4 produced nearly 65% removal under identical conditions. Likewise, green-synthesized ZnO nanoparticles by Alchornea laxiflora leaf extract exhibited 87% photocatalytic degradation of Congo red dye within 60 min, highlighting their dual potential for environmental and biomedical applications (Ekennia *et al.* 2021). The improved activity of composite were associated with its lower apparent bandgap, higher surface area, effective interfacial charge separation and improved visible-light utilization. Figure 7a compares time-dependent efficiencies of both photocatalysts. Figure 7b presents the corresponding spectra recorded using a Thermo Scientific spectrophotometer at approximately 500 nm. The progressive decline in the characteristic absorption band confirms gradual decomposition of Congo red.

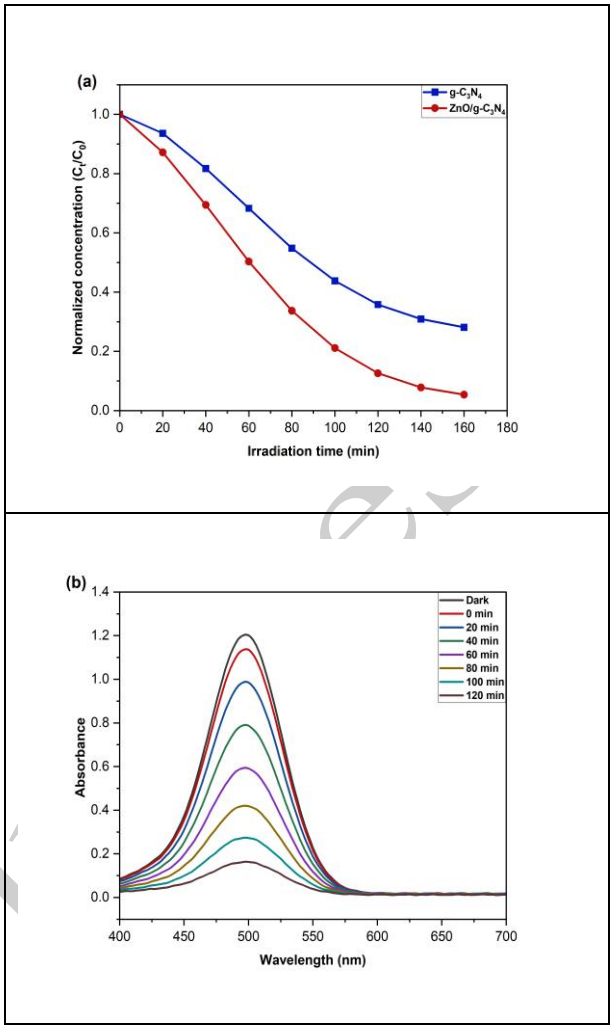

Fig. 7: (a) Time-dependent Congo red degradation; (b) corresponding spectral evolution profiles

Table 3. Comparative Congo red degradation efficiencies of synthesized photocatalysts

Sample	90 min (%)	120 min (%)
g-C_3N_4	51	65
ZnO/g-C_3N_4	73	87

3.3 Influence of Initial Congo Red Concentration

The influence of the starting Congo Red concentration was evaluated between 20 and 100 mg L^{-1} at natural pH using the optimized ZnO/g-C_3N_4 dosage of 0.04 g. As shown in Fig. 8a, approximately 97% degradation was obtained for 20 mg L^{-1} after 120 min. The removal efficiency declined to 86%, 75%, and 63% when the initial concentration was raised to 60, 80, and 100 mg L^{-1}, respectively.

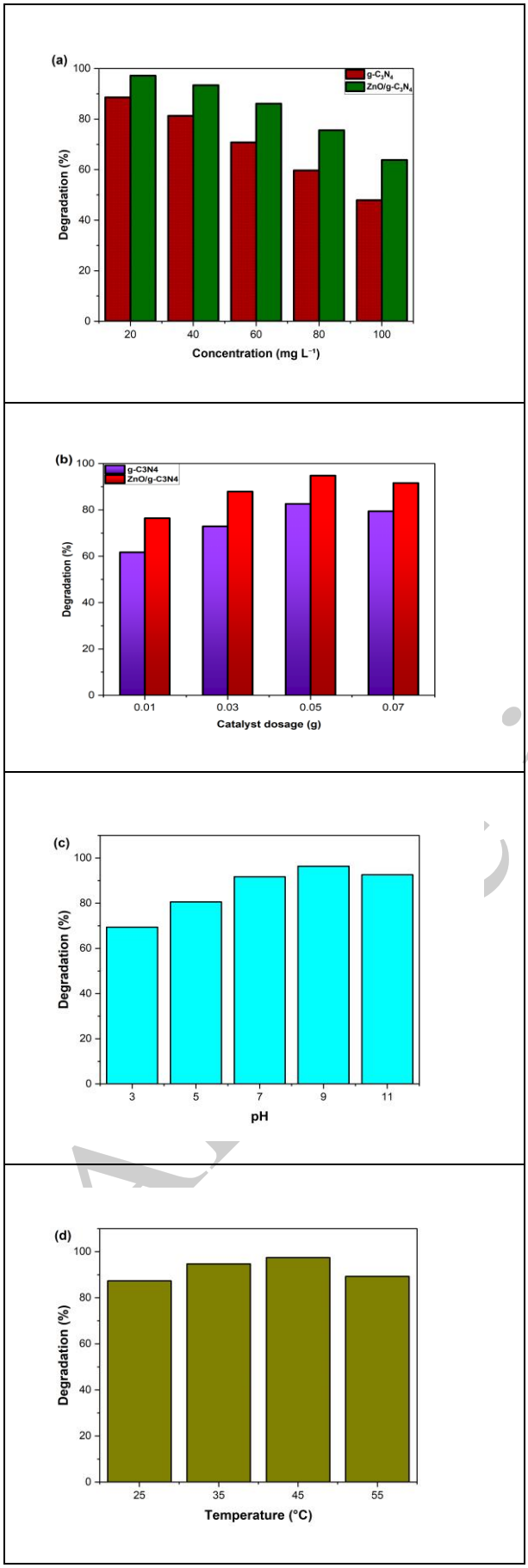

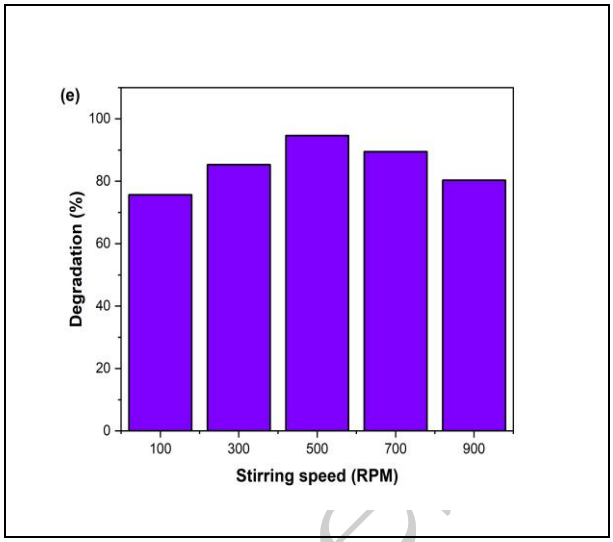

Fig. 8: Effects of (a) concentration, (b) dosage, (c) stirring (d) temperature, and (e) pH

At lower concentrations, the ratio of available photocatalytic sites to Congo red molecules was comparatively high, allowing efficient adsorption and oxidation. Increasing the pollutant concentration resulted in greater competition among molecules and transformation intermediates for the limited reactive sites. Moreover, concentrated dye solutions absorbed and scattered a larger fraction of the incident radiation. This inner-filter effect reduced light penetration through the suspension and limited photon absorption by the ZnO/g-C_3N_4 surface. Consequently, fewer photogenerated charge carriers and reactive oxygen species were produced, decreasing the overall degradation efficiency.

3.4 Influence of Photocatalyst Dosage

The effect of photocatalyst loading on Congo red degradation was examined using g-C_3N_4 and ZnO/g-C_3N_4. Increasing the dosage from 0.01 to 0.05 gram improved the removal performance because more illuminated surface sites became available for pollutant adsorption and reactive-species formation. At the optimum loading of 0.05 g, efficiencies of 82% and 95% were produced, respectively, after 120 min.

Increasing the loading to 0.07 g reduced the efficiencies to 79% and 91%, while dosages of 0.01 and 0.03 g resulted in 61% and 73% degradation, respectively. Excessive photocatalyst concentrations increased suspension turbidity, light scattering, and particle aggregation. These effects restricted photon penetration and reduced the effectively illuminated surface. Therefore, 0.05 g was selected as the optimum dosage for experiments. The outcomes were displayed in Figure 8b.

3.5 Influence of Solution pH

Solution pH strongly affects photocatalytic performance by modifying the surface charge of the photocatalyst, the ionization state of Congo red, and the production of reactive oxygen species. Because Congo red contains negatively charged sulfonate groups, its behaviour differs from that of cationic pollutants. The degradation efficiencies obtained at pH 3, 5, 7, 9, and 11 were approximately 69%, 80%, 91%, 96%, and 92%, respectively, after 90 min. In a previous study, Polypyrrole-coated titanium diboride (PPy@TiB_2) nanoparticles exhibited outstanding adsorption performance for Congo red dye, achieving 98.75% removal at pH 4 using a 60 mg adsorbent dose, while demonstrating excellent reusability and high adsorption capacity (Mayakannan *et al.* 2022).

The maximum efficiency at pH 5 was attributed to electrostatic attraction between protonated photocatalyst sites and the anionic pollutant molecules. At pH 3, excessive protonation, competing ions, and possible instability of surface Zn–O bonds slightly reduced activity. Under alkaline conditions, the increasingly negative photocatalyst surface repelled sulfonate groups, limiting adsorption and interfacial oxidation. Hydroxide-induced screening and radical side reactions may also contribute to the lower efficiencies. Consequently, mildly acidic conditions were most favourable for Congo red degradation. These results are presented in Fig. 8e.

3.6 Influence of Reaction Temperature

The temperature effect was evaluated from 25 to 55 °C while maintaining identical irradiation and reaction conditions. Congo red degradation increased from approximately 87% at 25 °C to 94% at 35 °C after 90 min. Moderate heating enhanced molecular diffusion, pollutant–surface collision frequency, and mass transfer between the solution and ZnO/g-C_3N_4 active sites.

Further temperature increases reduced the degradation efficiency to 97% at 45 °C and 89% at 55 °C. Excessive heating can weaken pollutant adsorption and shift the adsorption–desorption equilibrium toward the liquid phase. It may also reduce dissolved oxygen availability, thereby limiting the production of superoxide radicals. These effects outweighed the improvement in molecular mobility at higher temperatures.

3.7 Influence of Stirring Rate

The influence of mixing was investigated between 100 and 900 rpm. At 100 rpm, approximately 75% degradation was achieved because catalyst dispersion and pollutant transport were limited. Increasing the stirring rate to 300 and 500 rpm raised the efficiencies to 85% and 94%, respectively. A stirring rate of 500 rpm maintained a uniform suspension, restricted sedimentation, and improved mass transfer without generating excessive turbulence.

At 700 and 900 rpm, the degradation decreased to approximately 89% and 80%, respectively. Very rapid mixing can promote particle collisions and temporary aggregation while disturbing stable irradiation zones within the reactor. It may also introduce air bubbles that scatter incident light. Thus, 500 rpm was selected as the optimum stirring rate. The corresponding results are shown in Fig. 8c.

3.8 Reactive-species Trapping Experiments

Isopropyl alcohol was employed as a hydroxyl-radical scavenger, benzoquinone as a superoxide-radical quencher, and EDTA as a photogenerated-hole scavenger. Each compound was introduced at 10 mM under otherwise identical conditions. Pollutant concentrations were measured by a Thermo Scientific Evolution 220 UV spectrophotometer.

Without a scavenger, the composite achieved approximately 97% degradation. The addition of isopropyl alcohol reduced the efficiency to 76%, whereas EDTA lowered it to 83%. The strongest suppression was observed with benzoquinone, for which only 58% degradation was obtained. These findings show superoxide radicals ($O_2^{\cdot-}$) were the dominant oxidative species. Photogenerated holes (h^+) also contribute substantially, while hydroxyl radicals ($\cdot OH$) have a secondary role.

The proposed behaviour is consistent with interfacial charge transfer within $ZnO/g-C_3N_4$, which extends charge-carrier lifetimes and enables electrons to reduce dissolved oxygen into superoxide radicals. The resulting reactive species attack the azo linkage and aromatic structure of Congo red, producing smaller intermediates that undergo further oxidation.

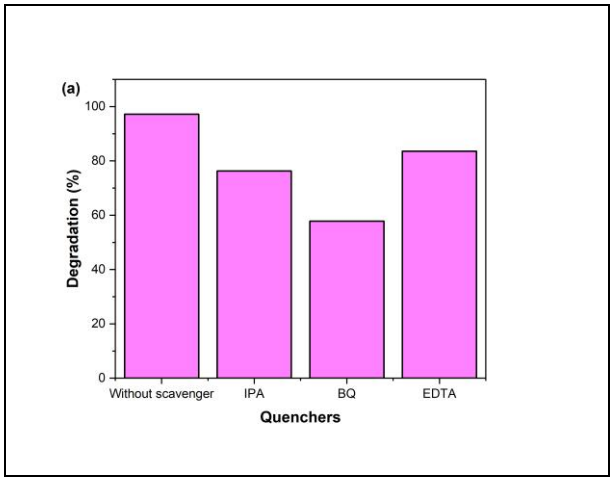

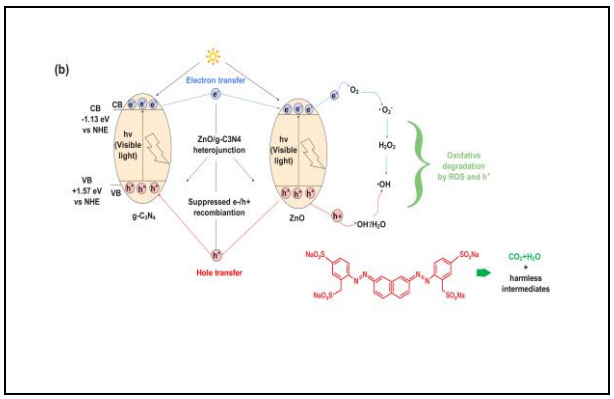

Fig. 9: (a) Reactive-species trapping results and (b) proposed Congo red degradation mechanism

3.9 Proposed Mechanism

Based on the trapping results, superoxide radicals ($O_2^{\cdot-}$) were considered the principal reactive species at Congo red degradation, while photogenerated holes (h^+) and hydroxyl radicals (●OH) provide additional contributions. At visible-light irradiation, $ZnO/g-C_3N_4$ heterojunction generates electron-hole and absorbs photons:

$$ZnO/g-C_3N_4 + h\nu \rightarrow e_{CB}^- + h_{VB}^+ \quad \ldots (4)$$

Interfacial charge migration restricts electron-hole recombination and preserves electrons with sufficient reducing ability on $g-C_3N_4$ conduction band.

$$e_{CB}^- + O_2 \rightarrow O_2^{\cdot-} \quad \ldots (5)$$

Superoxide species may undergo protonation and subsequent reactions that produce hydroxyl radicals and hydrogen peroxide (Ullah *et al.* 2025):

$$O_2^{\cdot-} + H^+ \rightarrow HO_2^{\cdot} \quad \ldots (6)$$

$$2HO_2^{\cdot} \rightarrow H_2O_2 + O_2 \quad \ldots (7)$$

$$H_2O_2 + e^- \rightarrow \cdot OH + OH^- \quad \ldots (8)$$

Meanwhile, holes remaining at valence band can oxidize hydroxide ions or adsorbed water and may also react directly with pollutant molecules:

$$h_{VB}^+ + H_2O \rightarrow \cdot OH + H^+ \quad \ldots (9)$$

$$h_{VB}^+ + OH^- \rightarrow \cdot OH \quad \ldots (10)$$

Generated reactive species attack the azo linkage, aromatic rings, and sulfonate-containing structure of Congo red. Successive oxidation produces smaller intermediates, followed by partial or complete mineralization:

$$\text{Congo red} + O_2^{\cdot-}/h^+/\cdot OH \rightarrow \text{intermediates} \rightarrow CO_2 + H_2O + \text{inorganic ions} \quad \ldots (11)$$

3.9.1 Photocatalytic Degradation Kinetics

Degradation kinetics of Congo red over the *Clerodendrum inerme*-assisted $ZnO/g-C_3N_4$ photocatalyst were interpreted using the Langmuir–Hinshelwood model for heterogeneous surface reactions. The overall process involves pollutant adsorption, photon-induced charge-carrier formation, generation of ROS, and oxidative decomposition of adsorbed molecules.

The general Langmuir–Hinshelwood rate expression is (Younas *et al.* 2024):

$$r = -\frac{dC}{dt} = \frac{k_r K_{ads} C}{1 + K_{ads} C} \quad \ldots (12)$$

where k_r were surface-reaction constant, K_{ads} shows adsorption-equilibrium constant, and C denotes Congo red concentration. At relatively low pollutant concentrations, $K_{ads}C \ll 1$; therefore, the relationship can be approximated by a pseudo-first-order expression:

$$-\frac{dC}{dt} = k_{app} C \quad \ldots (13)$$

Rearranging and integrating between C_0 at $t = 0$ and C_t at irradiation time t gives (Indira *et al.* 2021):

$$\frac{dC}{C} = -k_{app} dt \quad \ldots (14)$$

$$\int_{C_0}^{C_t} \frac{dC}{C} = -k_{app} \int_0^t dt \quad \ldots . (15)$$

$$\ln\left(\frac{C_0}{C_t}\right) = k_{app} t \quad \ldots (16)$$

$$C_t = C_0 e^{-k_{app} t} \quad \ldots (17)$$

Linear plots of $\ln(C_0/C_t)$ against irradiation time were generated initial concentrations between 20 and 80 mgL^{-1}. The apparent rate decreased 0.0356 to 0.0076 min^{-1} as concentration increased. This reduction resulted from stronger competition for active sites, increased light screening, and restricted photon penetration at elevated Congo red concentrations.

Table 4. Kinetic parameters derived from pseudo-first-order Congo red degradation

Initial Concentration (mgL^{-1})	k_{app} (min^{-1})	R^2
25	0.0356	0.999
50	0.0247	0.999
75	0.0148	0.999
100	0.0076	0.999

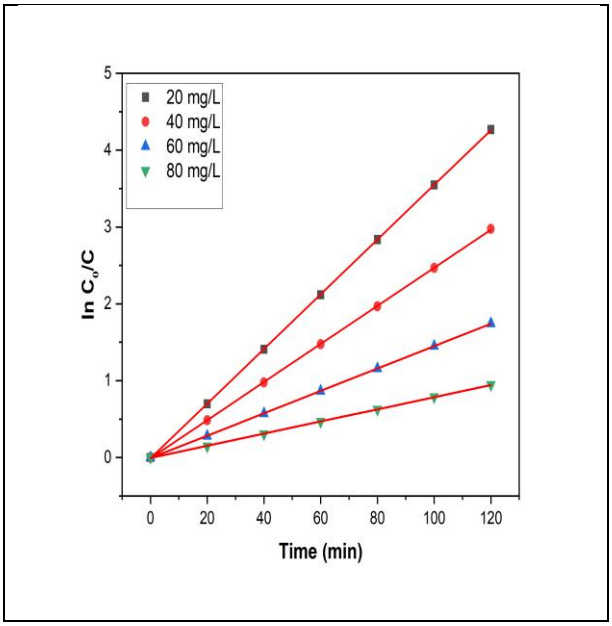

Fig. 10: Pseudo-first-order kinetic plots for concentration-dependent Congo red photodegradation

4. CONCLUSION

This study demonstrates an environmentally responsible route for preparing a ZnO/g-C_3N_4 heterojunction photocatalyst using *Clerodendrum inerme* leaf extract as a natural complexing and growth-controlling medium. The composite achieved 87% Congo red degradation within 120 min under visible-light irradiation, whereas g-C_3N_4 produced 65% removal under identical conditions. XRD confirmed coexistence of hexagonal wurtzite ZnO and layered g-C_3N_4 without detectable crystalline impurities. Heterojunction formation raised BET area from 90.0 to 107.0 $m^2 g^{-1}$ and lowered apparent bandgap from 2.68 to 3.13 eV, providing more accessible reaction sites and raised visible-light utilization. Reactive-species trapping showed that superoxide radicals was dominant oxidative species, with photogenerated holes and hydroxyl radicals contributing to Congo red decomposition. The reaction followed pseudo-first-order kinetics, and the best performance was obtained at 0.05g catalyst dosage, mildly acidic pH, and moderate temperature. Overall, prepared ZnO/g-C_3N_4 composite exhibited favourable efficiency and structural stability for dye-contaminated water treatment. Future investigations should evaluate mineralization, repeated-use stability, catalyst leaching, toxicity, and performance in real industrial wastewater containing mixed contaminants.

FUNDING

This research received no specific grant from any funding agency in the public, commercial, or not-for-profit sectors.

CONFLICTS OF INTEREST

The authors declare that there is no conflict of interest.

COPYRIGHT

REFERENCES

Alasmari, S. M., Albogami, B. Z. and Nenaah, G. E., Potential of using *Clerodendrum inerme* extracts, essential oil, and biosynthesized silver nanoparticles as ecofriendly natural pesticides for controlling the rust floor beetle, Tribolium castaneum infesting grain products in stores, *J. Stored Prod. Res.*, 114, 102715(2025a). https://doi.org/10.1016/j.jspr.2025.102715

Alasmari, S. M., Albogami, B. Z., Nenaah, G. E. and Nenaah, S. G., Bio-activities of *Clerodendrum inerme* extracts, essential oil, main terpenes and Ag nanoparticles against the stable fly, Stomoxys calcitrans (Diptera: Muscidae) and their non-target effects against its parasitoid, Spalangia cameroni (Hymenoptera: Pteromalidae) and earthworms, *Veteri. Parasitol.*, 337, 110497(2025b). https://doi.org/10.1016/j.vetpar.2025.110497

Al-Enazi, N. M., Optimized synthesis of mono and bimetallic nanoparticles mediated by unicellular algal (diatom) and its efficiency to degrade azo dyes for wastewater treatment, *Chemosphere*, 303, 135068(2022). https://doi.org/10.1016/j.chemosphere.2022.135068

Amale, A. B., Satishkumar, P., Bhagat, P. R., Motghare, M. S. and Krishnaraj, C., Green Synthesis of ZnO Nanoparticles Using Azadirachta indica Leaf Extract for Rapid Catalytic Degradation of Organic Pollutants, *J. Environ. Nanotechnol.*, 15(2), 151–161 (2026). https://doi.org/10.13074/jent.2026.06.2612082

Anuradha, G., Snega, S., Dinesh, R. and Manimekalai, R., Dendrophthoe falcata extract mediated Fe_3O_4 nanoparticles: A functional agent for dye degradation and inflammation mitigation, *J. Mol. Struct.*, 1319, 139433(2025). https://doi.org/10.1016/j.molstruc.2024.139433

Chauhan, A., Verma, R., Dhatwalia, J., Kumari, A., Dutta, V., Chandrasekaran, G., Ghotekar, S., Kaur, M., Vignesh, J. and Thakur, S., Phyto-mediated synthesis of pure phase α-Bi_2O_3 nanostructures using

Rubus ellipticus plant extract: photocatalytic activity and antimicrobial efficacy, *Biomass Convers. Biorefin.*, 14(20), 25103–25122 (2024). https://doi.org/10.1007/s13399-023-04679-8

Dahiya, S., Sharma, R., Gautam, P., Panchal, P., Chaudhary, S., Sharma, A., Almáši, M. and Nehra, S. P., Eco-friendly phytofabrication of Ficus Benjamina L. based ZnO-doped g-C_3N_4 nanocomposites for remarkable photocatalysis and antibacterial applications, *Chemosphere.*, 339, 139707(2023). https://doi.org/10.1016/j.chemosphere.2023.139707

Ekennia, A., Uduagwu, D., Olowu, O., Nwanji, O., Oje, O., Daniel, B., Mgbii, S. and Emma-Uba, C., Biosynthesis of zinc oxide nanoparticles using leaf extracts of Alchornea laxiflora and its tyrosinase inhibition and catalytic studies, *Micron*, 141, 102964(2021). https://doi.org/10.1016/j.micron.2020.102964

Ganvir, H. V, Musrif, P. G., Satishkumar, P., Kadam, A. D., Saminathan, R. and Krishnaraj, C., Sustainable Synthesis of MgO Nanoparticles from *Clerodendrum inerme* Bast Fiber Extract: Physicochemical Characterization and Antibacterial Performance, *J. Environ. Nanotechnol.*, 15(2), 380–388 (2026). https://doi.org/10.13074/jent.2026.06.2622227

Hao, J., Wen, Y., Jiao, Y., Zhao, Z., E, H., Wang, J., Wang, S., Zuo, M., Liu, J., Cui, S. and Yang, X., Enhanced photocatalytic deoxynivalenol degradation using ZnO/g-C_3N_4 S-scheme heterojunction, *Chem. Phy. Lett.*, 882, 142459(2026). https://doi.org/10.1016/j.cplett.2025.142459

Hassan, F., Backer, S. N., Almanassra, I. W., Ali Atieh, M., Elbahri, M. and Shanableh, A., Solar-matched S-scheme ZnO/g-C_3N_4 for visible light-driven paracetamol degradation, *Sci. Rep.*, 14(1), 12220(2024). https://doi.org/10.1038/s41598-024-60306-0

Indira, K., Shanmugam, S., Hari, A., Vasantharaj, S., Sathiyavimal, S., Brindhadevi, K., El Askary, A., Elfasakhany, A. and Pugazhendhi, A. Photocatalytic degradation of congo red dye using nickel–titanium dioxide nanoflakes synthesized by Mukia madrasapatna leaf extract, *Environ. Res.*, 202, 111647(2021). https://doi.org/10.1016/j.envres.2021.111647

Kashyap, D. N., Shalom, N., Mayakannan, S., Muthuraj, M., Thanikasalam, A. and Ahmed, A. A., Comparative Green and Wet-chemical Synthesis of ZnO Nanoparticles: Enhanced Photocatalytic and SERS Performance of Defect-rich Nanostructures, *J. Environ. Nanotechnol.*, 15(2), 162–175 (2026). https://doi.org/10.13074/jent.2026.06.2612090

Khan, Z. U. H., Khan, A., Shah, N. S., Din, I. U., Salam, M. A., Iqbal, J., Muhammad, N., Imran, M., Ali, M., Sayed, M. and Gohar, M. A., Photocatalytic and biomedical investigation of green synthesized NiONPs: Toxicities and degradation pathways of Congo red dye, *Surf. Interf.*, 23, 100944(2021). https://doi.org/10.1016/j.surfin.2021.100944

Khawale, V. R., Kumar, R., Satishkumar, P., Haldar, B., Deepa, B., Saminathan, R., Veeramanikandan, P., Packirisamy, A. S. B. and Selvaraju, M., Study on Electrochemical Stability and Charge Transfer Efficiency for the Development of High-Performance Supercapacitors Using Iron Oxide (Fe_2O_3) Nanorods, *J. New Mater. Electrochem. Syst.*, 27(3), 163–171 (2024). https://doi.org/10.14447/jnmes.v27i3.a01

Langa, C., Mabuba, N., Mahlaule-Glory, L. M., Motaung, D. E., Tetana, Z. and Hintsho-Mbita, N. C., Enhanced photocatalytic degradation of dyes and pharmaceutical pollutants using Fe/TiO_2-carbon nanospheres from Sutherlandia Frutescence, *Int. J. Environ. Anal. Chem.*, 106(4), 790–820 (2026). https://doi.org/10.1080/03067319.2025.2524833

Langa, C., Mathipa, M., Mabuba, N. and Hintsho-Mbita, N. C., Effect of calcination temperature on the structural and photocatalytic properties of nickel sulfide nanoparticles for dye degradation and antibacterial applications, *Chem. Phy. Impact*, 11, 100913 (2025). https://doi.org/10.1016/j.chphi.2025.100913

Lekshmi, G. S., Ramasamy, T., Bazaka, O., Levchenko, I., Bazaka, K., Govindan, R. and Mandhakini, M., Antioxidant, Anti-Bacterial, and Congo Red Dye Degradation Activity of AgxO-Decorated Mustard Oil-Derived rGO Nanocomposites, *Mol.*, 27(18), 5950 (2022). https://doi.org/10.3390/molecules27185950

Mathialagan, A., Manavalan, M., Venkatachalam, K., Mohammad, F., Oh, W. C. and Sagadevan, S., Fabrication and physicochemical characterization of g-C_3N_4/ZnO composite with enhanced photocatalytic activity under visible light, *Opt. Mater.*, 100, 109643 (2020). https://doi.org/10.1016/j.optmat.2019.109643

Mayakannan, S., Rathinam, R., Saminathan, R., Deepalakshmi, R., Gopal, M., Hillary, J. J. M., Nanthakumar, S., Ganvir, V. Y. and Singh, P., Analysis of Spectroscopic, Morphological Characterization and Interaction of Dye Molecules for the Surface Modification of TiB_2 Nanoparticles, *J. Nanomater.*, 2022(1), 1033216 (2022). https://doi.org/10.1155/2022/1033216

Mohanta, Y. K., Mishra, A. K., Panda, J., Chakrabartty, I., Sarma, B., Panda, S. K., Chopra, H., Zengin, G., Moloney, M. G. and Sharifi-Rad, M., Promising applications of phyto-fabricated silver nanoparticles: Recent trends in biomedicine, *Biochem. Biophy. Res. Commun.*, 688, 149126(2023). https://doi.org/10.1016/j.bbrc.2023.149126

Prajapati, A. K. and Mondal, M. K., Novel green strategy for CuO–ZnO–C nanocomposites fabrication using marigold (Tagetes spp.) flower petals extract with and without CTAB treatment for adsorption of Cr(VI) and Congo red dye, *J. Environ. Manage.*, 290, 112615(2021). https://doi.org/10.1016/j.jenvman.2021.112615

Prisrin, S. A., Priyanga, M., Ponvel, K. M., Kaviarasan, K. and Kalidass, S., Plant Mediated Approach for the Fabrication of Nano CuO–NiO Mixed Oxides Using Aqueous Extract of Mimusops Elengi Leaf: Green Synthesis, Characterization and Antibacterial Activity Studies, *J. Clust. Sci.*, 33(2), 765–772 (2022). https://doi.org/10.1007/s10876-021-02016-5

Senthilkumar, S. and Govindasamy, K., Green Synthesis of Mn-Doped ZnO Nanoparticles Using *Ipomoea Staphylina* Leaf Extract: Characterization and Application of Photocatalytic Dye Degradation, Antibacterial and Antioxidant Activity, *Chem. Select*, 9(35), e202402347(2024). https://doi.org/10.1002/slct.202402347

Ullah, M. A., Robel, F. N., Bahadur, N. M., Bashar, M. S., Khan, S., Ahmed, M. F., Ahmed, S. and Sahadat Hossain, M., Plant Extract-Mediated Synthesis of Nano-Crystallite TiO_2 for the Efficient Photocatalytic Degradation of Textile Effluent and Antibiotics, *Chem. Asian J.*, 20(23), e00352 (2025). https://doi.org/10.1002/asia.202500352

Utomo, W. P., Afifah, P. A. I., Rozafia, A. I., Mahardika, A. A., Santoso, E., Liu, R. and Hartanto, D., Modulation of particle size and morphology of zinc oxide in graphitic carbon nitride/zinc oxide composites for enhanced photocatalytic degradation of methylene blue, *Surf. Interf.*, 46, 104017(2024). https://doi.org/10.1016/j.surfin.2024.104017

Van Thuan, D., Nguyen, T. B. H., Pham, T. H., Kim, J., Hien Chu, T. T., Nguyen, M. V, Nguyen, K. D., Al-onazi, W. A. and Elshikh, M. S., Photodegradation of ciprofloxacin antibiotic in water by using ZnO-doped g-C_3N_4 photocatalyst, *Chemosphere*, 308, 136408(2022). https://doi.org/10.1016/j.chemosphere.2022.136408

Younas, M. U., Usman, A., Kashif, A. R., Zahoor, A. and Haider, F., Green Synthesis of TiO_2 NPs Using Agave americana Leaves: Antioxidant, Cytotoxicity, and Photocatalytic Activity, *Chem. Select*, 9(44), e202404050 (2024). https://doi.org/10.1002/slct.202404050